ELSEVIER

Journal of Fluids and Structures 25 (2009) 343–363

JOURNAL OF FLUIDS AND STRUCTURES

www.elsevier.com/locate/jfs

Unsteady free surface wave-induced separation: Vortical structures and instabilities

M. Kandasamy, T. Xing, F. Stern*

Iowa Institute of Hydraulic Research, University of Iowa, Iowa City, IA 52242-1585, USA

Received 20 June 2007; accepted 16 May 2008
Available online 17 July 2008

Abstract

Vortical structures and instability mechanisms of the unsteady free surface wave-induced separation around a surface-piercing NACA0024 foil at a Froude number of 0.37 and a Reynolds number of 1.52×10^6 are studied using an unsteady Reynolds-averaged Navier–Stokes (URANS) code with a blended $k-\varepsilon/k-\omega$ turbulence model and a free surface tracking method. At the free surface, the separated flow reattaches to the foil surface resulting in a wall-bounded separation bubble. The mean and instantaneous flow topologies in the separation region are similar to the owl-face pattern. The initial shear-layer instability, the Karman-like instability, and the flapping instability are identified, and their scaling and physical mechanisms are studied. Validation with experimental fluid dynamics (EFD) and comparison with complementary detached-eddy simulation (DES) indicate that URANS resolves part of the organized oscillations due to the large-scale unsteady vortical structures and instabilities, thereby capturing the gross features of the unsteady separation. The URANS solutions show an initial amplitude defect of 30% for the free surface oscillations where the shear layer separates, and the defect progressively increases downstream as URANS rapidly dissipates the rolled up vortices.

Keywords: Unsteady 3-D separation; Instability analysis; Vortex dynamics; Topological analysis; URANS

1. Introduction

Three-dimensional (3-D) flow separation is a vast area of study, which is not yet fully understood. The free surface adds to complications due to the waves and their interaction with boundary layers and vortices, free surface turbulence, and air–water interfacial effects such as bubble entrainment and surface tension. In some cases, adverse piezometric pressure gradients due to steep waves induce and/or modify boundary layer separation. Gaining insight into the fluid mechanics of these areas would be of both fundamental and practical interest, especially regarding applications in ship and ocean engineering.

Historically, the investigation of steady 3-D separation has been conducted through topological analysis, which provides a framework to classify the separation and deduce the volume flow field based on the nodes, saddles, and the lines of separation and attachment on the surface streamlines. Although it is rarely used for analyzing unsteady

*Corresponding author.
E-mail address: Frederick-stern@uiowa.edu (F. Stern).

0889-9746/$ - see front matter © 2008 Elsevier Ltd. All rights reserved.
doi:10.1016/j.jfluidstructs.2008.05.002

3-D separation, topological analysis can still be performed at instantaneous time steps to elucidate the transport properties of the vortices in the separation region (Post et al., 2003).

Typically, unsteady separation is analyzed by studying the different instability mechanisms associated with the organized oscillations due to large-scale vortical structures. For non-reattaching separated shear layers such as in flow past circular cylinder and spheres, the main instabilities are the shear-layer instability and the Karman instability. For reattaching separated shear layers such as in flow past the blunt leading edge of cylinders and backward-facing steps, the main instabilities are the shear-layer instability, the "Karman-like" shedding instability caused by amalgamation of the shear-layer vortices, and the flapping instability.

The shear-layer instability initiates at a critical Reynolds number (Re) which depends on the spatial restrictions imposed by the mean recirculation length, i.e., at least one wavelength has to fit into the recirculation length and the instability should have reached a significant level of amplification. For cylinder flows, a large disparity exists in the literature for the precise value of the critical Re (~350–3000) due to additional effects of free-stream turbulence and the span-wise end conditions (Prasad and Williamson, 1997). The frequency f_S of the shear-layer instability, which is similar to a Kelvin–Helmholtz instability, scales with the momentum thickness of the shear layer at separation θ such that the normalized Strouhal number is given by $St_\theta = f_S\theta/U_S$, where U_S is the shear-layer velocity at separation. Ripley and Pauley (1993) demonstrated computationally that St_θ is independent of Re in the range $113\,928 < Re < 364\,747$ for separated laminar boundary layers over airfoils. However, they concluded that St_θ varies with the nondimensional pressure distribution and it therefore is geometry dependent.

The primary wake instability for non-reattaching separation like in the case of circular cylinders is the Karman instability, which is caused by the interaction between the two opposite vortices. The Karman instability initiates at Re~49 and is evident even after the boundary layer transitions to turbulence at $Re \sim 10^6$ (Williamson, 1996). The Karman shedding frequency f_K scales with the distance between the separated shear layers. Roshko (1955) found that the normalized Strouhal number, $St_h = f_K h/U_S$, where h is the half-wake thickness, has a universal value of 0.08, and is independent of both Re and the geometry.

For separation with wall-bounded separation bubbles like in the case of backward-facing steps (Lee and Sung, 2002) and flow past the blunt leading edge of cylinders (Sigurdson, 1995), the shear-layer vortices amalgamate together to form large-scale vortices that impinge on the wall just after the recirculation region, interact with the mirror image, and shed. Although the vortex interaction is with its mirror image, unlike the staggered vortical arrangement of the Karman vortices, Sigurdson (1995) showed that the scaling factors remain the same, the equivalent h in this case being the normal distance of the separated shear layer from the wall. Henceforth, we shall use the term "Karman-like" shedding for such type of symmetric vortex shedding for wall-bounded bubbles. For the Karman-like shedding, St_h mostly varies between 0.07 and 0.09 for different geometries (Sigurdson, 1995).

Another significant difference between the free separation bubbles and wall-bounded separation bubbles is the existence of a stationary recirculation region for the latter case, which exhibits a periodic enlargement and shrinkage that has been termed as the "flapping" instability. This type of instability has a standing-wave-type nature (Kiya and Sasaki, 1985). The general consensus is that the flapping frequency f_F scales with the mean reattachment length X_R, such that the normalized Strouhal number is given by $St_R = f_F X_R/U_\infty$, where U_∞ is the inlet velocity. For flow past the blunt leading edge of cylinders (Kiya and Sasaki, 1985), $St_R = 0.12$ with $X_R = 10\ R_C$ (R_C is the cylinder radius). For flow past backward-facing steps (Lee and Sung, 2002), $St_R = 0.1$ with $X_R = 7.4\ H_S$ (H_S is the step height). For flow past a 2-D square rib (Liu et al., 2008), $St_R = 0.073$ with $X_R = 9.75\ H_R$ (H_R is the rib height); measurements of the instantaneous reattachment point in response to the flapping motion indicated an oscillation of $0.12\ X_R$ about the mean X_R.

The applicability of unsteady Reynolds-averaged Navier–Stokes (URANS) to simulate these instabilities has been studied for a few basic geometries with mixed results. In the context of triple decomposition, URANS is assumed capable of resolving the unsteady mean flow, i.e., the mean and organized oscillations flow field, while the random fluctuations are modeled as Reynolds stresses. Generally, URANS relies on the existence of a spectral gap between the time scales of the unsteady mean flow and the random fluctuations, thus separating the resolved and modeled time scales. However, measurements of spectra for most bluff body flows indicate an absence of the spectral gap. Under such circumstances where the resolved and modeled scales of motion overlap, the URANS eddy viscosity model, unlike large-eddy simulation (LES), fails to account for the scales of motions already resolved by the particular grid, and hence does not reduce the eddy viscosity accordingly. This leads to an excessive artificial dissipation that over-damps the resolved scales of motion, causing an amplitude defect. In many cases, the smallest scales of organized motions, namely the shear-layer vortices are completely smeared out by the eddy viscosity. Constantinescu et al. (2003) did a comparative study of numerical simulations of the sub-critical flow over a sphere using URANS with different turbulence models, LES, and detached-eddy simulation (DES) at $Re = 10^4$. The URANS models predicted the value of the Karman shedding frequency accurately, but with an amplitude defect, and completely failed to predict the formation of shear-layer vortices. Nevertheless, even in the absence of a spectral gap, researchers have shown the ability

of URANS to predict the shear-layer vortices for other geometries. Khorammi et al. (2001) used URANS with the $k-\omega$ turbulence model for the acoustic analysis on the cove region of a cambered slat, and were able to predict the formation and the subsequent development of the free shear-layer instabilities that were responsible for the radiated noise. Comparison with experimental measurements showed a good correspondence for the frequency spectrum, although the amplitude of the computed noise was about 30% smaller than the measured values. Paik et al. (2004) did a comparative study using URANS with the Spalart–Allmaras turbulence model and DES for flow past a corner mounted rectangular block and found that URANS yields unsteadiness within the shear layer. The location of the major peaks in the power spectrum distribution agreed well with the DES simulations, albeit with an amplitude defect greater than 50%. Thus, the ability of URANS to predict the shear-layer vortices is case dependent and relies on whether the length and time scales of the shear-layer vortices are large enough to overcome the excessive damping effects of the modeled eddy viscosity.

Few studies have investigated the effects of free surface on the instabilities associated with unsteady 3-D separation, and they have mainly focused on the Karman instability. Kawamura et al. (2002) performed LES simulations for flow past surface-piercing circular cylinders. Simulations at Froude number (Fr) = 0.8 showed that at the deep regions Karman shedding occurs, but near the free surface large-scale interactions between the two separated shear layers become less prominent due to the deformation of the free surface. The conjecture was that the inclination of the separated shear layers due to the presence of waves hampers large-scale vortex shedding. The region in which the vortex shedding is hampered extends to about one diameter from the mean water level. Lin and Li (2003) performed LES simulations for flow past surface-piercing square cylinders and demonstrated that the presence of waves can reduce both the vortex strength and frequency of the Karman vortex shedding induced by a uniform current due to the nonlinear wave–current interaction.

Related, but unique is the separation induced solely by the free surface waves where the deep flow remains attached. Most of the work on this type of separation has focused on the mean flow separation pattern and topological analysis. Detailed analysis of the instability mechanisms governing the unsteadiness has not been performed until now. This type of separation was first identified by Chow (1967) through an experimental fluid dynamics (EFD) study using a surface-piercing foil designed for insignificant separation for the deep condition. Chow showed that the separation occurred at medium and high Fr, initiated just beyond the wave trough and extended to the foil trailing edge. Subsequently, Stern et al. (1989) identified the existence of this type of separation in their EFD study on the effects of waves on the boundary layer of a surface-piercing flat plate with a superposed Stokes wave generated by an attached upstream-submerged horizontal hydrofoil. The separation occurred at high wave steepness, initiated beyond the wave trough, and extended to the plate trailing edge. Using the same flow geometry, Stern et al. (1993) performed laminar Navier–Stokes computations, which magnified the separation size due to the increased three-dimensionality and response to pressure gradients, and thus facilitated the analysis of the flow topology based on critical point concepts. The laminar solutions showed an outward spiral node on the free surface with a saddle point on the plate. The global flow topology resembled the owl-face pattern (Perry and Chong, 1987), but with one less node–saddle combination on the foil surface. Zhang and Stern (1996) performed steady RANS simulations using a Baldwin–Lomax turbulence model with free surface-tracking method on a surface-piercing NACA24 foil at $\mathrm{Fr} = 0.37$ and $\mathrm{Re} = 1.52 \times 10^6$. This geometry allowed for a more prominent separation at the turbulent regime compared to the Stern et al. (1989, 1993) geometry, thereby facilitating more detailed experiments and topological analysis of the turbulent solutions. The flow topology was similar to Stern et al. (1993), showing global topological similarity to the owl-face pattern, but with extra critical points on the foil surface. Complementary EFD wave-profile ζ_p measurements at the intersection of the foil and the free surface showed an abrupt rise in the free surface wave-elevation ζ just after the bow wave trough (toe), at which point the flow separates with vertical oscillations amounting to 15% of the ζ dynamic range in the separation region. Pogozelski et al. (1997) is the only experimental work that analyzes the volume flow field for such flows. They conducted experiments using a surface-piercing foil and constructed a sketch of the flow structure based on video images and PIV measurements at one spatial orientation for $\mathrm{Fr} = 0.25$ and $\mathrm{Re} = 6.8 \times 10^5$. Sketches depict stream-wise counter rotating vortex pairs occurring close to the free surface, which begin with shoulder wave breaking. Unfortunately, analysis was limited to $\mathrm{Fr} = 0.25$ at which there was no flow reversal, whereas all the other related studies have focused on separation with flow reversal at higher Fr. The authors point out that flow reversal is evident for $\mathrm{Fr} > 0.30$ but measurement was not made due to the number of entrained bubbles making velocity measurement difficult. Steady RANS by Kandasamy (2001) with a second-order finite difference method using a blended $k-\omega/k-\varepsilon$ turbulence model and improved free surface tracking on the same geometry and flow conditions as Zhang and Stern (1996) showed better comparison of the mean ζ and foil surface C_P with complementary EFD by Metcalf (2001). The flow topology was similar to the owl-face pattern. Subsequently, Metcalf et al. (2006) identified certain dominant periodic modes from the EFD frequency spectra of ζ and the foil surface C_P for $\mathrm{Fr} = 0.37$, but the flow physics behind these frequencies could not be explained since the complexity of the separation made detailed volume flow measurements difficult.

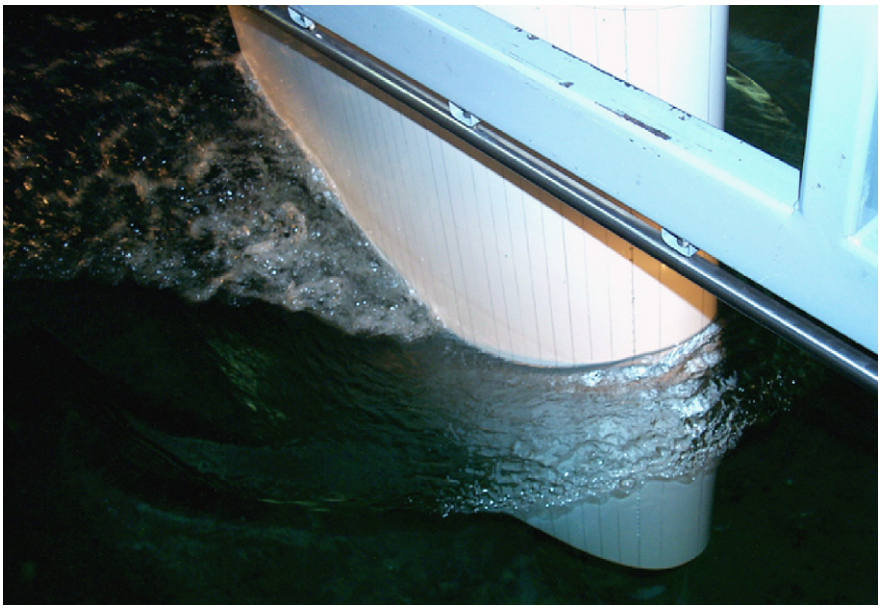

Fig. 1. Surface-piercing NACA24 foil at Fr = 0.37.

The current study extends the previous steady RANS studies to URANS in order to explain the instability mechanisms behind the dominant periodic modes identified in the EFD measurements, as part of a complementary URANS and DES study using both surface-tracking and level-set approaches. This paper focuses on the URANS with tracking approach, which was the first to be performed. The turbulence-generated disturbances in the free surface are not modeled, as they require a two-phase level-set approach with specialized boundary conditions (Brocchini, 2002). The free surface eruptions in Fig. 1 indicate that the broken free surface is a result of the strong turbulence generated underneath the free surface meeting the free surface (Brocchini and Peregrine, 2001). Triple decomposition of the unsteady free surface elevation spectra by Metcalf et al. (2006) shows that the average root mean square (r.m.s.) of the visually prominent random fluctuations is an order of magnitude smaller than that of the underlying organized oscillations in the separation region. The turbulence-induced free surface eruptions would affect the evolution of turbulent eddies of similar and lower time scales in the inertial and dissipation ranges of the energy spectrum. However, its effect on the organized oscillations occurring in the energy containing range, which is the focus of the current study, is small. The current approach proved capable in capturing the instabilities driving the organized oscillations, but with a significant amplitude defect. Solutions obtained using URANS with level-set approach failed to capture the instabilities due to the additional dissipation from the reinitialization of the level-set function, which compounds with the already dissipative nature of URANS. The complementary DES study (Xing et al., 2007) focused primarily on the level-set approach because of the difficulty in achieving a monotonically converged solution using the surface-tracking approach, which is attributed to the limiter on the maximum wave slope required by the surface-tracking method. The DES study supports findings from the current URANS study, and highlights the relative advantages and disadvantages of the different computational methods. The difficulty in isolating and visualizing the vortical structures from the many small-scale eddies in DES established that need for URANS, which damps the random fluctuations and resolves only the large-scale organized oscillations albeit with deficiencies in their amplitudes. The main similarities and differences of the current URANS solutions with respect to the DES solutions will be discussed in the concluding remarks.

2. Computational method

The general-purpose parallel URANS solver, CFDShip-Iowa, has been developed at the Iowa Institute of Hydraulic Research over the past 15 years. Documentation of the basic method, URANS with the blended $k-\varepsilon/k-\omega$ turbulence model and the DES turbulence model using the free surface-tracking method (version 3.03), is provided in Wilson et al. (2006). Version 3.03 has been extended to version 4.0 (Carrica et al., 2006) with the use of the single-phase level-set method. The current paper uses version 3.03 of the code with the URANS and surface-tracking method, whereas

Xing et al. (2007) focuses on the DES with level-set using version 4. The following provides a brief description of the URANS and surface-tracking method used.

2.1. Governing equations

For Cartesian coordinates, the continuity equation and the momentum equation in the nondimensional tensor form are

$$\frac{\partial U_i}{\partial x_i} = 0, \tag{1}$$

$$\frac{\partial U_i}{\partial t} + U_j \frac{\partial U_i}{\partial x_j} = -\frac{\partial \hat{p}}{\partial x_j} + \frac{1}{\mathrm{Re}} \frac{\partial^2 U_i}{\partial x_j \partial x_j} - \frac{\partial}{\partial x_j} \overline{u_i u_j}. \tag{2}$$

All equations are nondimensionalized using the reference velocity U_0 (towing speed of the foil = 1.27 m/s), the foil length $L = 1.2$ m, and the water density $\rho = 998\,\mathrm{kg/m^3}$ (average water temperature 19 °C). $U_i = (U, V, W)$ are the dimensionless Reynolds-averaged velocity components, $x_i = (x, y, z)$ are the coordinate directions, t is the dimensionless flow time, $\hat{p} = p_{\mathrm{abs}}/\rho U_0^2 + z/\mathrm{Fr}^2$ is the piezometric pressure coefficient, $\mathrm{Re} = U_0 L/\nu$ is the Reynolds number, ν is the molecular viscosity $= 1.00263 \times 10^{-6}\,\mathrm{m^2/s}$ (average water temperature 19 °C), $\mathrm{Fr} = U_0/\sqrt{gL}$ is the Froude number, and $\overline{u_i u_j}$ are the Reynolds stresses which are two-point correlation of the random fluctuations u_i.

2.2. Turbulence

The Reynolds stresses are directly related to the mean rate-of-strain through an isotropic eddy viscosity ν_t as expressed in

$$-\overline{u_i u_j} = \nu_t \left(\frac{\partial U_i}{\partial x_j} + \frac{\partial U_j}{\partial x_i} \right) - \frac{2}{3} \delta_{ij} k, \tag{3}$$

where δ_{ij} is the Kronecker delta and $k = \frac{1}{2} u_{ii}$ is the turbulent kinetic energy. Substituting (3) for the Reynolds-stress term in (2) gives the modified momentum equation:

$$\frac{\partial U_i}{\partial t} + U_j \frac{\partial U_i}{\partial x_j} = -\frac{\partial P}{\partial x_j} + \frac{1}{R_{\mathrm{eff}}} \frac{\partial^2 U_i}{\partial x_j \partial x_j} - \frac{\partial \nu_t}{\partial x_j} \left(\frac{\partial U_i}{\partial x_j} + \frac{\partial U_j}{\partial x_i} \right); \tag{4}$$

$P = \hat{p} + \frac{2}{3} k$ and $1/R_{\mathrm{eff}} = 1/\mathrm{Re} + \nu_t$, and ν_t are computed using a blended k–ε/k–ω model (Menter, 1994). A blending function is designed to be unity in the viscous sublayer and logarithmic regions of boundary layers, where the k–ω model is set active, and gradually switches to zero in the wake region, where the k–ε model is set active, to take advantage of the strengths of both the models. The k–ω model does not require near-wall damping functions and uses simple Dirichlet boundary conditions while the k–ε model does not exhibit sensitivity to the level of free-stream turbulence, as does the k–ω model.

2.3. Free surface

The computational domain covers the water region only and the grid is dynamically conformed to the free surface location. The kinematic free surface boundary condition given by Eq. (5) updates the grid every time step to compute ζ (expressed dimensionless henceforth) and requires that the free surface is a material surface

$$\frac{\partial \zeta}{\partial t} + U \frac{\partial \zeta}{\partial x} + V \frac{\partial \zeta}{\partial y} - W = 0. \tag{5}$$

At the intersection of the free surface and no-slip surface (i.e., the contact line), Eq. (5) becomes singular when the contact line is in motion but the fluid velocity is zero due to the viscous no-slip boundary condition. To overcome the problem, a small near-wall region is "blanked out" when solving Eq. (5) and the solution in this region is linearly extrapolated from the interior of the domain. The dynamic free surface boundary condition requires that the stresses are continuous at the free surface, and provides the boundary conditions for velocity and pressure, which will be provided in forthcoming sections.

2.4. Numerical method

All the solutions presented in this paper use the third-order finite difference scheme for the spatial discretization of the momentum equation, as the second-order scheme dissipates the shear-layer vortices too rapidly, and fails to predict their subsequent amalgamation. A second-order finite difference scheme is used for the temporal discretization. The pressure implicit split operator algorithm used uses a predictor-corrector approach to advance the momentum equation while enforcing the continuity equation. Fourth-order artificial dissipation implicitly added by taking a linear combination of full- and half-cell operators (Sotiropoulos and Abdallah, 1992) overcomes the pressure velocity-decoupling problem caused by the collocated grid. The overall method is fully implicit, and a line-ADI (alternating direction implicit) scheme with a pentadiagonal solver and under-relaxation is used to solve the algebraic equations. A message-passing interface-based domain decomposition approach is used, where each decomposed block is mapped to one processor of a parallel IBM SP 3 supercomputer.

2.5. Geometry and flow conditions

Fig. 1 shows a photo of the foil at $Fr = 0.37$ and $Re = 1.52 \times 10^6$ in the tow tank. The tow tank dimensions are $w/L = 2.5$ and $h/d_f = 2$ (where w is the width of tow tank, h the depth of tow tank, and d_f the foil draft). To reduce computational cost, instead of modeling the exact tow tank conditions, the foil is modeled with an extended foil draft ($2d_f$) where the foil reaches the bottom boundary with no flow beneath the foil, and without the towing tank walls (Fig. 2). The extended foil draft prevents the restricted water effects due to the bottom from affecting the free surface solutions. In the tow tank, there is flow beneath the foil along its flat bottom, which forms a separation bubble near the leading edge affecting the pressure distribution near the foil bottom and the local flow. Previous CFD and EFD established relatively small dependence of the free surface separation pattern to both the wall and the foil bottom (Kandasamy, 2001).

Simulations with quantitative verification and validation were conducted for all three experimental conditions covering minimal, reattaching, and non-reattaching separation: $Fr = 0.19$, 0.37, and 0.55 with respective $Re = 0.78 \times 10^6$, 1.52×10^6, and 2.26×10^6, as provided by Kandasamy (2005). Herein, only the $Fr = 0.37$ results are presented since this is the condition at which the most extensive EFD validation data are available, and at which the DES was conducted. Laminar simulations (both 2-D and $Fr = 0.37$, at $Re = 1500$ and 2500) were also conducted to compare St_θ and St_h with that of the turbulent simulations. The laminar simulations also enabled comparison of St_θ and St_h at the free surface with respective values for the deep-flow separation, since the deep flow does not separate for the turbulent simulations.

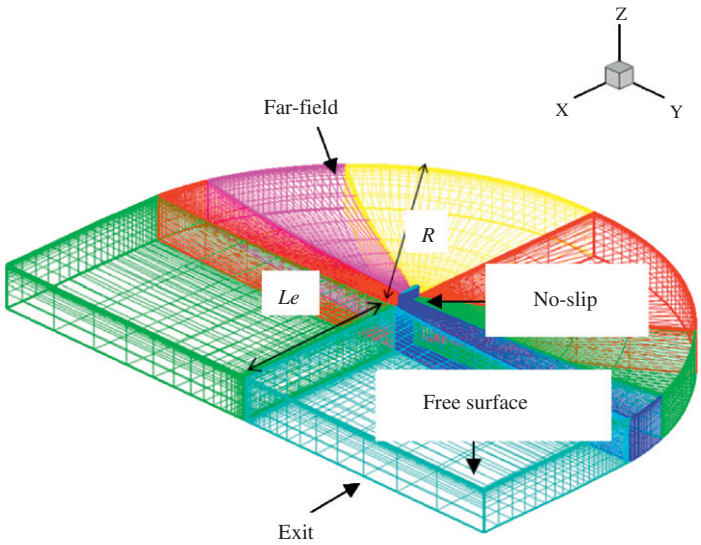

Fig. 2. Computational domain, boundary conditions, and grid topology.

2.6. Computational domain and grids

The foil, with a dimensionless length of 1, extends from $x = 0$ to 1. The body-fitted C-grid (Fig. 2) was decomposed into 8 separate blocks for parallel computation. The grid has a far-field boundary that is a semicircle of radius $R = 10$ encircling the foil with the trailing edge ($x = 1$) as its focal point. A rectangular grid of length $Le = 8$ and width $2R$ extends from the trailing edge to the exit. The domain size was finalized based on results from domain convergence studies. Three domains with $R = 5$, 7, and 10 with respective $Le = 5.5$, 6.6, and 8 were used in the study. The nondimensional mean coefficient of total resistance C_{TX} converged with a convergence ratio of 0.6, with a 0.15% difference between the largest two grids. The wall coordinate $y+ = U_\tau y/\nu$, where U_τ is the friction velocity, was kept less than 1 for all grids. The grid is clustered near the free surface too, with an initial grid spacing less than 10^{-3} for all the grids. The grids were generated using the commercial code GRIDGEN.

Note that the current simulations use a full domain, whereas Xing et al. (2007) use a half-domain. The full domain was created in order to consider the very low-frequency asymmetric meandering wake in the far field. However, the analysis of the far-field wake proved difficult since the running mean of the side forces did not converge to zero even after 80 flow times on the fine grid. It is reasonable to expect that a much larger domain size and a much longer running time will be required to resolve this meandering wake, which is beyond the affordable computer resources and scope of the current study.

2.7. Boundary conditions

The boundary conditions specified on each boundary are as follows. On the foil surface, a no-slip condition is used, i.e., $(U, V, W) = 0$ and the pressure gradient is assumed to be zero, i.e., $\partial P/\partial n = 0$ (where n is normal to the boundary). On the exit plane, axial diffusion and pressure gradient are assumed to be zero, i.e., $\partial^2(U, V, W)/\partial x^2 = 0$ and $\partial P/\partial x = 0$. On the bottom deep boundary, an impenetrable slip condition is used, i.e., $\partial(U, V, P)/\partial z = 0$ and $W = 0$. On the outer boundary, a far-field boundary condition is used, i.e., $U = U_o$, $V = 0$, $W = 0$, and $P = 0$. On the free surface, the dynamic free surface boundary condition dictates that $\partial(U, V, W)/\partial z = 0$ and $\hat{p} = \zeta/\mathrm{Fr}^2$. The conditions on the turbulent quantities are as follows: on the foil surface, $k = 0$, $\omega = 60/(\mathrm{Re} \times 0.075 \times \Delta y^2)$, $v_t = 0$; on the exit plane, on the bottom deep boundary, on the outer boundary, and on the free surface $\partial k/\partial n = 0$, $\partial\omega/\partial n = 0$, and $\partial v_t/\partial n = 0$.

2.8. Analysis methods

The fast Fourier transform (FFT) of ζ and the foil surface C_P time histories enabled the identification of the frequencies corresponding to the different instability mechanisms, and helped isolate regions where the different instabilities dominate in the flow field. The time evolution of the vortices was studied at the locations corresponding to the different frequencies identified, and the instability mechanisms were related to the evolution of the extracted vortices. The vortices were extracted using two different vortex extraction techniques, the Q criterion (Hunt et al., 1988) and velocity vector eigenmodes vortex detection (Sujudi and Haimes, 1995). The first method is based on the balance between the rotation rate and the strain rate, and positive Q iso-surfaces denote regions where the strength of rotation overcomes the strain thus making those surfaces eligible as vortex envelopes. The main disadvantage of this method is the difficulty in distinguishing the individual vortices. The second method is based on the extraction of vortex core lines. This method distinguishes the individual vortices, but sometimes has difficulty in producing contiguous vortex core lines. The individual limitations of these two methods were overcome by using the two together. The accuracy of the detected vortices was ascertained by seeding streamlines near vortex cores and visualizing the swirling patterns that are generally associated with vortices. The topology of separation at different instantaneous time steps was also analyzed to investigate the behavior of the critical points during events such as vortex merger and breakdown.

3. Verification and validation

Verification and validation used Stern et al. (2001) methodology and procedures with updated correction factors by Wilson et al. (2004). Verification is a process for assessing the simulation numerical uncertainty U_{SN} given by $U_{SN}^2 = U_I^2 + U_T^2 + U_G^2$, where U_I is the iterative uncertainty, U_T is the time-step uncertainty, and U_G is the grid uncertainty. Validation is the process for assessing the simulation modeling uncertainty by comparing with experimental data D. The comparison error E is given by the difference between D and the simulation S. To determine if the solutions are validated, E is compared to the validation uncertainty U_V, given by $U_V^2 = U_D^2 + U_{SN}^2$,

Table 1
Grids used for verification

Grids	1	2	3	4	5 (Non-systematic final solution grid)
Size	70 680	114 048	187 824	531 006	1 004 400
$y+$	0.36	0.3	0.25	0.18	0.9

Table 2
Grid studies for C_{TX}

Case	Grids	r_G	p_G	U_{SN} (%)
1	1, 2, 3	1.189	1.94	15
2	1, 3, 4	1.414	2.9	4

where U_D is the uncertainty in the data. If $|E| < U_V$, the combination of all the errors in D and S is smaller than U_V and validation is achieved at the U_V level. Metcalf et al. (2006) provide data for the mean ζ and the mean foil surface C_P. In addition, the time history of ζ and the foil surface C_P are available over 10 flow times after the initial transients have subsided. This enables quantitative comparisons of the r.m.s. and the FFT for both ζ and the foil surface C_P.

Tables 1 and 2 summarize the grids used for the grid studies and the different studies conducted, respectively. Two separate grid studies were conducted: Case 1 using refinement ratio $(r_G) = \sqrt[4]{2}$, and Case 2 using $r_G = \sqrt{2}$. The verification of point variables (ζ and C_P) poses a problem at locations where the solution changes approach zero such that convergence ratio ($R_G = \varepsilon_{32}/\varepsilon_{21}$, where ε_{32} and ε_{21} are the solution changes between the fine grid and medium grid, and the solution changes between medium grid and coarse grid, respectively) approaches zero. To overcome this problem, separate L2 norms of ε_{21} and ε_{32} over ζ_p were used to define ratios for R_G. The same R_G value was used in calculating point-wise U_{SN} for ζ_p, ζ, and C_P. U_V and E were calculated and the point variables were validated using grid-4. Grid densities were determined considering initial understanding of flow physics and computer resources, prior to detailed analysis of results. A finer non-systematic grid (grid-5) was generated with an improved grid distribution to better capture the features identified from the grid-4 solutions. The solutions from grid-5 lie within the validation uncertainty intervals of the grid-4 solutions for both C_{TX} and the point variables (ζ_p, ζ, and C_P), and were used for the analysis of the unsteady separation pattern.

3.1. Iterative and statistical convergence

Parametric studies on sub-iterations (free surface/momentum coupling) for each time step ensured iterative solution convergence at each time step. Results showed difference of 5% and $<1\%$ for C_{TX} by changing free surface/momentum coupling iterations from 3 to 4, and 4 to 5, respectively. Simulations then used 4 free surface/momentum coupling iterations. Statistical convergence of the running average on the time histories of C_{TX} established statistically stationary unsteady solutions. The criterion for statistical convergence is that the magnitude of fluctuations of the running mean drop to less than 1% of the mean value., i.e., $U_I < 1\%$ mean C_{TX}.

3.2. Time-step studies

Time-step studies were conducted on grid-3 (Case 1 fine grid) for C_{TX} with a refinement ratio of $\sqrt{2}$ ($\Delta t = 0.00707$, 0.01, and 0.014). The results show oscillatory convergence for C_{TX} with the time-step uncertainty ($U_T = 0.3\%$ of mean C_{TX}) similar in magnitude as U_I, both being an order of magnitude smaller than U_G for Case 1. $U_T \sim U_I \ll U_G$, so that simulation numerical uncertainty $U_{SN} = \sqrt{(U_G{}^2 + U_T{}^2 + U_I{}^2)} \sim U_G$.

3.3. Verification of C_{TX}

Table 2 tabulates results from grid studies for mean C_{TX}. For Case 1, the order of accuracy p_G (= 1.94) is lower than the theoretical order of accuracy p_{Gth} (= 3) with $U_{SN} = 15\%$, indicating that the asymptotic range is not reached. For

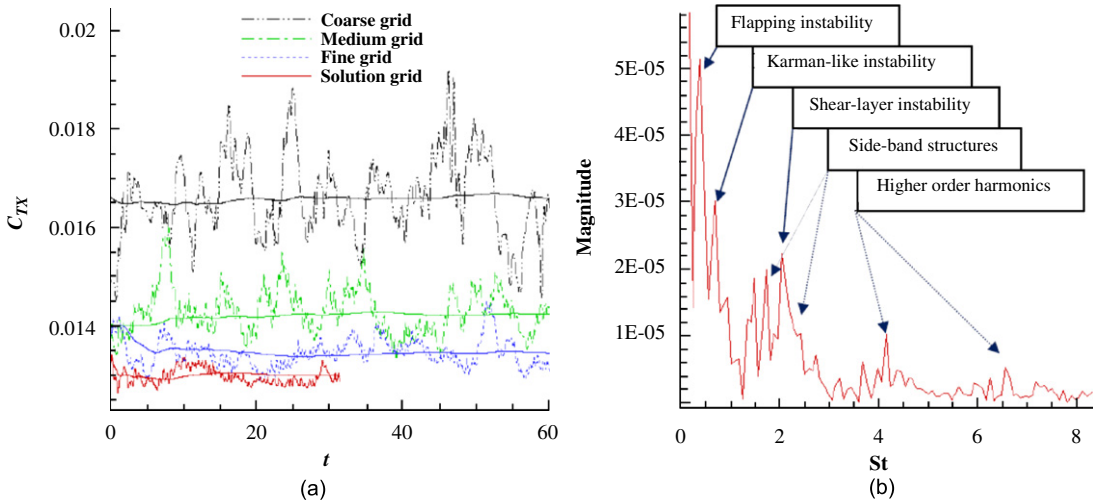

Fig. 3. C_{TX}: (a) time history of the solutions on all four grids; (b) FFT of the solution grid time history.

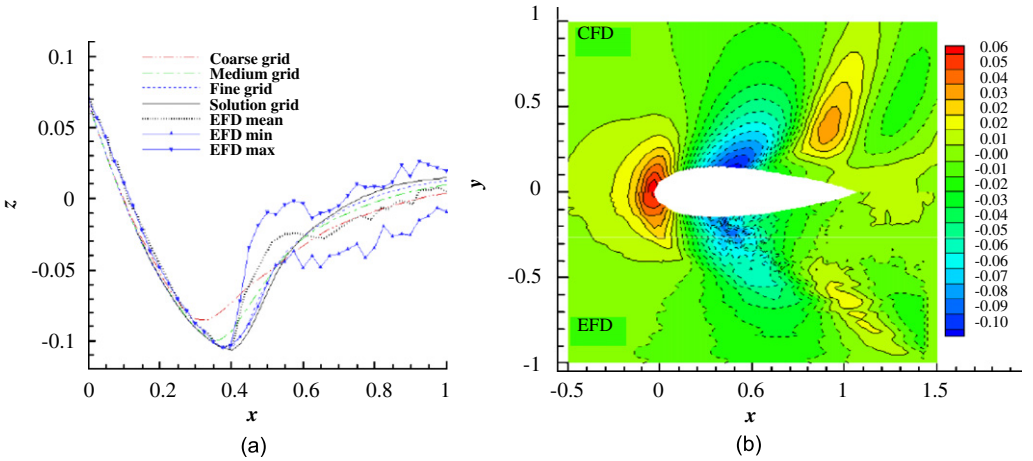

Fig. 4. Validation of mean ζ: (a) ζ_p on all grids and EFD data; (b) ζ on solution grid and EFD data.

Case 2, p_G (= 2.9) is close to p_{Gth}, and the uncertainties are much lower compared to Case 1 with $U_{SN} = 4\%$. Fig. 3(a) shows the grid convergence of the C_{TX} running mean for Case 2 grid study, along with the C_{TX} for grid-5 (solution grid). The mean C_{TX} for the solution grid is 0.013, which lies within the uncertainly interval of grid-4. No EFD data are available for the validation of C_{TX}. Fig. 3(b) shows the spectra of the general Strouhal number given by $\mathrm{St} = fL/U_0$, obtained by performing an FFT of the solution grid C_{TX} time history. The FFT shows the highest peaks around St = 0.3, 0.7, and 2, corresponding to the "flapping", "Karman-like", and the shear-layer instabilities, respectively, which will be discussed in forthcoming sections. The multiple primary instability modes interact non-linearly to produce sum and difference frequency modes, which in turn interact with the primary instability modes producing more sum and difference frequency modes (Miksad et al., 1982). This process continues, causing spectral broadening and the occurrence of the side-banded structures adjacent to the primary instability modes as seen in Fig. 3(b). The second and third harmonics of the shear-layer instability frequency are also distinctly evident in Fig. 3(b).

3.4. Verification, validation, and discussion of point variables

Fig. 4(a) shows ζ_p for the three grids used in the Case 2 grid study, along with the solution grid and EFD profiles. Monotonic convergence is achieved, but with p_G (= 1.8) less than p_{Gth}, which is consistent with expectations for solutions on stretched, curvilinear grids. EFD depicts the toe at $x = 0.4$ with an abrupt recovery ($x = 0.4$–0.5), followed

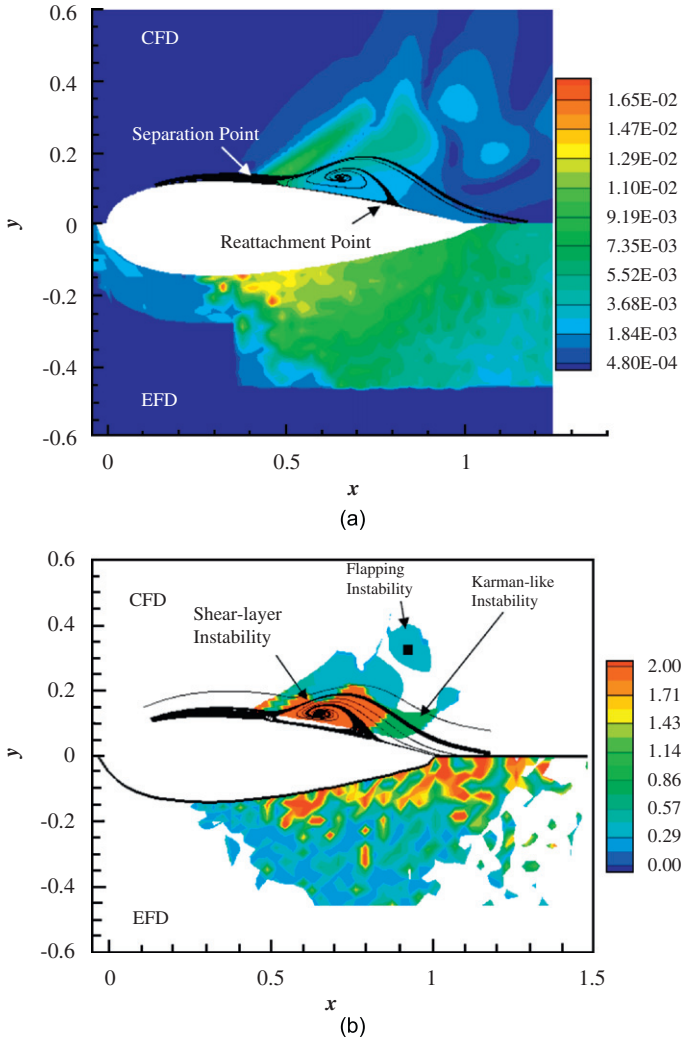

Fig. 5. Validation of unsteady ζ: (a) r.m.s., separation bubble illustrated in the CFD contour; (b) dominant St; the square location marker on the CFD plot indicates location at which point-wise comparisons will be presented for the flapping instability (Fig. 10).

by a more gradual recovery with oscillations further downstream ($x \geqslant 0.5$). URANS predicts the location of the toe accurately, but fails to predict the subsequent sharp rise in ζ_p. This causes an under-prediction of ζ_p at $0.4 < x < 0.6$ and an over-prediction of ζ_p at $x > 0.6$. Fig. 4(b) compares ζ between CFD and EFD over the entire free surface domain. EFD shows that the Kelvin wave is displaced away from the foil surface by the separation region. The Kelvin wave is not displaced far enough in CFD since URANS predicts a smaller separation region. The wave amplitudes are also higher in CFD. $|E|$ exceeds U_V by 15% at the toe and by 10% along the Kelvin wave crest.

Fig. 5(a) compares the r.m.s. of ζ between CFD and EFD. The superposed free surface mean flow streamlines illustrate the separation bubble at the free surface in the CFD contour plot. EFD shows that the r.m.s. peaks near the toe with significant values of r.m.s. in a semi-elliptical region near the shoulder, which roughly corresponds to the shape of the separation bubble illustrated in the CFD. The CFD r.m.s. values compare better when the shear layer first separates with about 30% amplitude defect [(CFD−EFD)/EFD × 100%], but the defect increases downstream as URANS rapidly dissipates the rolled up vortices. Fig. 5(b) shows contours of St corresponding to the dominant frequency (most energy containing frequency) on the free surface. The contours have a cut-off St of 0.25 based on the non-dimensional time window ($t = 10$) used for the FFT. The low r.m.s. regions have been blanked out to eliminate noise. EFD data indicate that the regions of most significant r.m.s. are dominated by shear-layer and Karman-like

shedding frequency, whereas in the outer region, flapping frequency is also found along with many points with intermittent or broad-banded frequencies. Unlike EFD, CFD shows a clear demarcation between the different instabilities. Three distinct regions are evident: a high-frequency ($St = 2$) region within the separation region where the shear-layer instability dominates, an intermediate frequency ($St = 0.74$) region immediately after reattachment where the karman-like instability dominates, and a low-frequency ($St = 0.32$) region enveloping the separation region where the flapping instability dominates. URANS diminishes the strength of the predicted Karman-like vortices, which are characterized by lower r.m.s., due to the rapid dissipation of the shear-layer vortices before amalgamation. The stronger "Karman-like" instability in the EFD and the resulting stronger non-linear interaction with the shear-layer instability result in the intermittent nature of the dominant frequency contours within the separation region. The exact orientation of the separated shear layer is not evident from the EFD for comparison, but it should be noted that the $k-\varepsilon$ turbulence model under-predicts the level of the turbulent stresses in the detached shear layer emanating from the separation line and hence sometimes predict a smaller separation region (Johnson et al., 1994). The square marker on the CFD plot indicates the location at which point-wise comparisons will be presented for the flapping instability.

Figs. 6(a) and (b) compare the foil surface C_P between EFD and CFD, respectively. The CFD solutions were interpolated into the EFD data acquisition grid to facilitate validation. EFD shows that the free surface effects penetrate to $z = -0.3$ and the bottom effects are evident for $z < -0.7$ with a nearly 2-D pressure coefficient for the intermediate depths. The foil surface C_P reaches a minimum near the toe, and recovers more gradually near the free surface compared to the deep flow due to the separation. CFD predicts a comparatively quicker pressure recovery at the free surface, indicating a smaller separation size compared to EFD. This results in a high comparison error near the reattachment region and validation was not achieved at the reattachment region as $|E|$ exceeds U_V by 16%. Note also that the foil bottom effects lead to an increase in C_P close to the foil bottom in the EFD contours which is not modeled in CFD.

Fig. 7(a) compares the r.m.s. of the foil surface C_P between EFD and CFD. The dotted lines on the CFD plots indicate the boundary of the EFD data acquisition points. EFD shows that significant r.m.s. magnitudes are for a semi-elliptical-shaped region initiating just beyond the wave trough and extending to the trailing edge with a penetration depth up to $z = -0.25$. The CFD predicts a similar semi-elliptical-shaped region of high r.m.s., but with amplitude defect. Fig. 7(b) shows the St corresponding to the dominant frequency on the foil surface for EFD and CFD. EFD data indicate that the regions of most significant r.m.s. are dominated by shear-layer and Karman-like shedding frequency. CFD shows three distinct regions corresponding to the three main instabilities. The shear-layer instability dominates in the separation region, the Karman-like instability dominates after reattachment, and the flapping instability dominates underneath the separation region. Due to the rapid dissipation of the shear-layer vortices, their subsequent amalgamation and shedding in the form of "Karman-like" vortices is significantly damped, and hence the contour plots indicate an overwhelming dominance of the shear-layer instability. The circle and diamond markers on the CFD plot indicate locations at which point-wise comparisons will be presented for the shear-layer and Karman-like instabilities, respectively. The pressure taps used in the EFD on the foil surface are relatively sparse below $z = 0.15$, and hence the frequency corresponding to the flapping instability is not apparent.

Figs. 8(a) and (b) provide an EFD/CFD comparison of the fluctuations of C_P about the mean and the corresponding frequency spectra, respectively, at the location (x, $z = 0.69$, -0.11) indicated by the circle location marker in Fig. 7(b). The time markers on the CFD plot in Fig. 8(a) indicate instances in the shear-layer shedding time-period T_S at which details of the volume flow will be illustrated in forthcoming sections. The band-averaged FFT is presented in Fig. 8(b) to smooth out the spike clusters and enable clearer identification of the most prominent frequencies. The EFD frequency spectrum depicts a peak at $St = 1.6$, and CFD depicts a corresponding peak at $St = 2$. The magnitude of the peak in the EFD spectra is two times higher than that of CFD. Figs. 9(a) and (b) provide an EFD/CFD comparison of the fluctuations of C_P about the mean and the corresponding frequency spectra, respectively, at the location (x, $z = 0.86$, -0.14) indicated by the diamond location marker in Fig. 7(b). The time markers on the CFD plot in Fig. 9(a) indicate instances in the Karman-like shedding time-period T_K at which details of the volume flow will be illustrated. The EFD frequency spectrum depicts a dominant peak at $St = 0.7$ corresponding to the Karman-like instability and another lower-magnitude peak at $St = 2$ corresponding to the shear-layer instability. The CFD frequency spectrum depicts a dominant peak at $St = 0.74$ and a peak of slightly lower magnitude at $St = 2$. Though the CFD shows a close match of the Strouhal numbers, the amplitudes are roughly four times lower. Figs. 10(a) and (b) provide an EFD/CFD comparison of the fluctuations of ζ about the mean and the corresponding frequency spectra, respectively, at the location (x, $y = 0.90$, 0.32) denoted by the square location marker in Fig. 5(b). The time markers on the CFD plot in Fig. 10(a) indicate instances in the flapping time-period T_F at which flow details will be illustrated. The EFD and CFD depict peaks at $St = 0.38$ and 0.32, respectively. URANS predicts the amplitude of the flapping frequency accurately (less than 1% difference), indicating that the

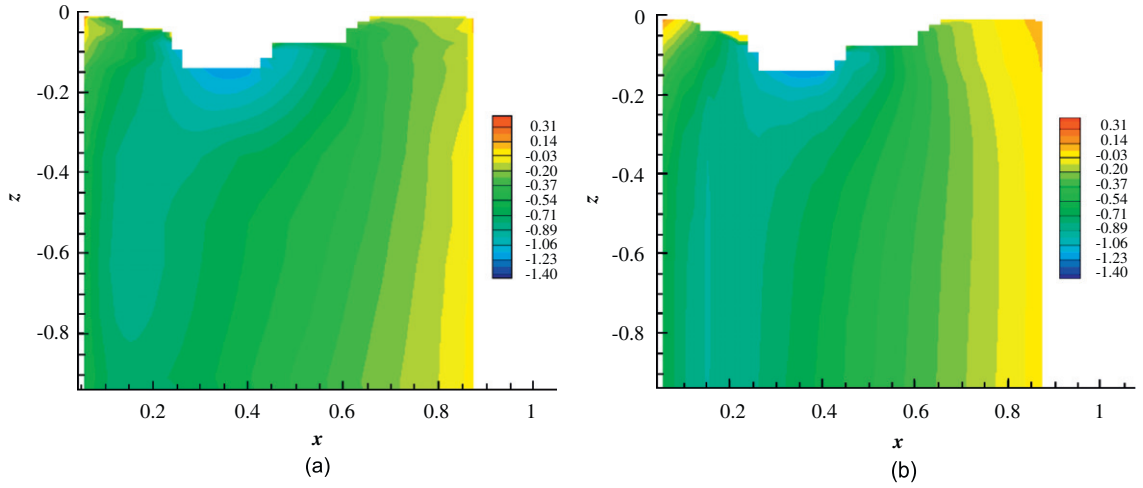

Fig. 6. Validation of mean C_P: (a) EFD and (b) CFD.

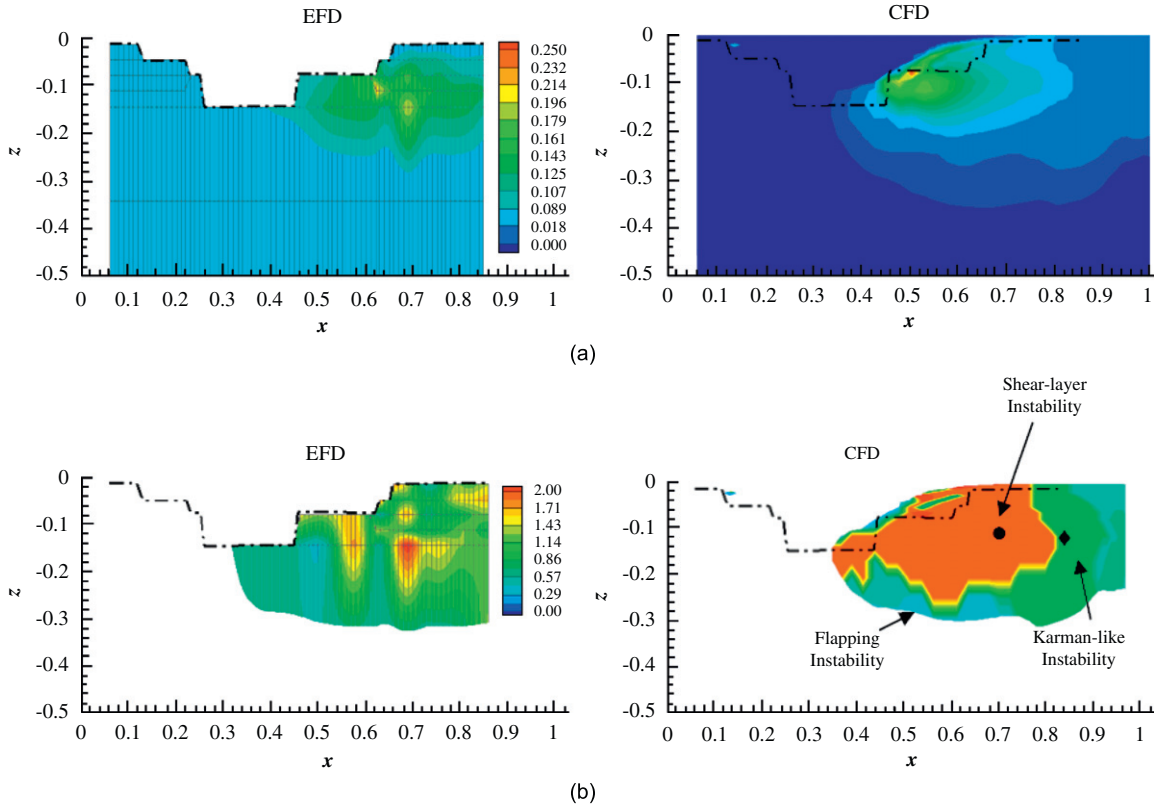

Fig. 7. Validation of unsteady C_P: (a) r.m.s.; (b) dominant St; the circle and diamond location markers on the CFD plot indicate locations at which point-wise comparisons will be presented for the shear layer (Fig. 8) and Karman-like instabilities (Fig. 9), respectively.

excessive dissipation of URANS has little effect on this standing-wave-type instability. The spectral broadening due to nonlinear interactions is evident in all the EFD and CFD frequency spectra, with the EFD showing stronger interactions.

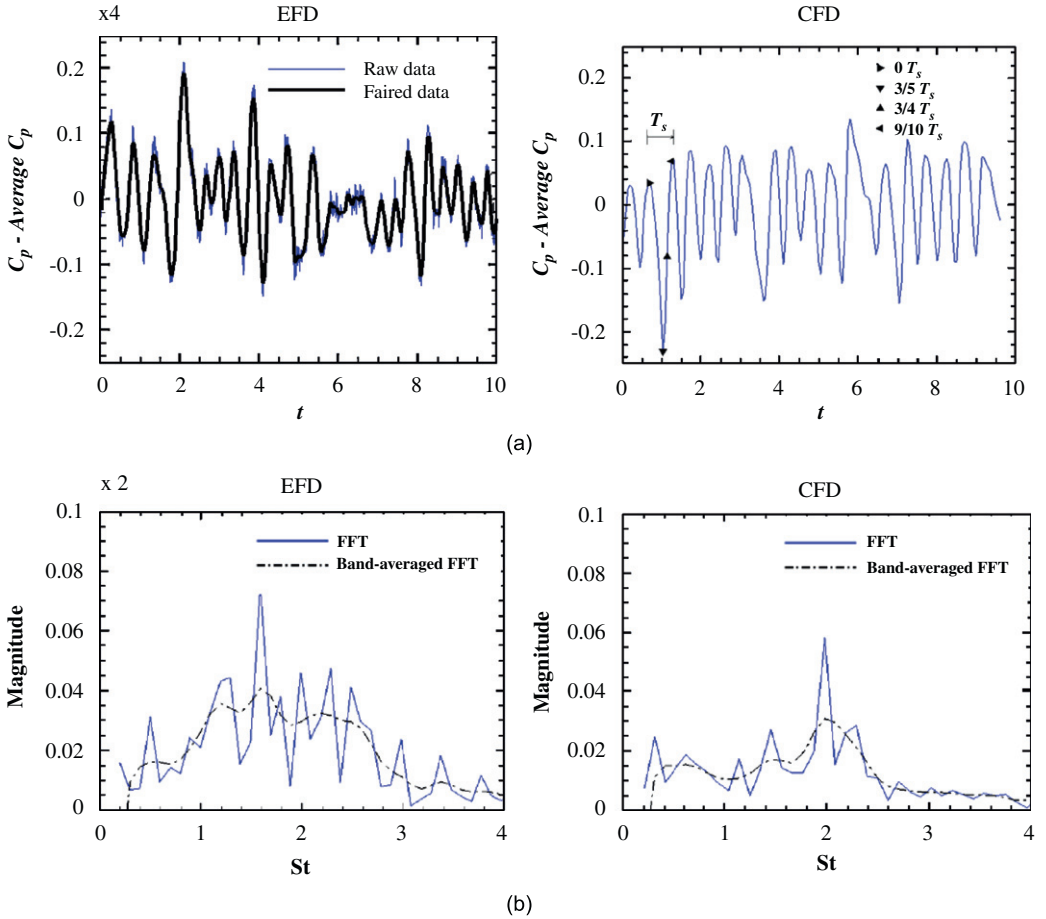

Fig. 8. Validation of unsteady C_P at location of dominant shear-layer instability ($x = 0.69$, $z = -0.11$) denoted by the circle location marker in Fig. 7 (b): (a) time history; CFD time markers indicate instances at which detailed volume flow will be presented in Fig. 12; (b) frequency spectra.

4. Mean separation pattern

Fig. 11 shows the mean separation pattern. The shear layer separates at the free surface at $x = 0.40$, and reattaches at $x = 0.82$ forming a wall-bounded separation bubble. At the toe, the stagnation C_P decreases to 58% of the original level at the leading edge due to dissipation, which agrees with Pogozelski et al. (1997) who report a decrease of 50–60% for their case. Assuming that the flow outside the separation region is inviscid, the iso-surface of the stagnation C_P at the toe ($= 0.29$), immediately before separation, gives an approximate visualization of the separated shear layer (iso-surface in Fig. 11(a)). The surface streamlines at the free surface and the foil surface (Fig. 11(b)) illustrate the owl-face topological pattern. The volume flow is interrogated by using the velocity vector eigen-modes vortex detection (vortex core line contoured by non-dimensional vortex strength), the Q criterion (iso-surfaces of $Q = 1$ shown), and volume streamlines. All three visualization methods show vortical flow transporting fluid from the inward spiral node on the foil surface to the outward spiral node on the free surface. The vortex strength along the vortex core decreases as it nears the free surface. The iso-surface of positive Q resembles an inverted "V" shape, which shows an additional structure after reattachment that traces the path of the Karman-like vortices. The velocity vector eigen-modes method fails to detect this vortical structure due to its weak nature.

5. Instantaneous separation patterns and instability analysis

The overall unsteady separation exhibits a similar behavior as that observed for other reattaching flows with wall-bounded separation bubbles. The initial shear-layer instability causes the separated shear layer to roll up and form the

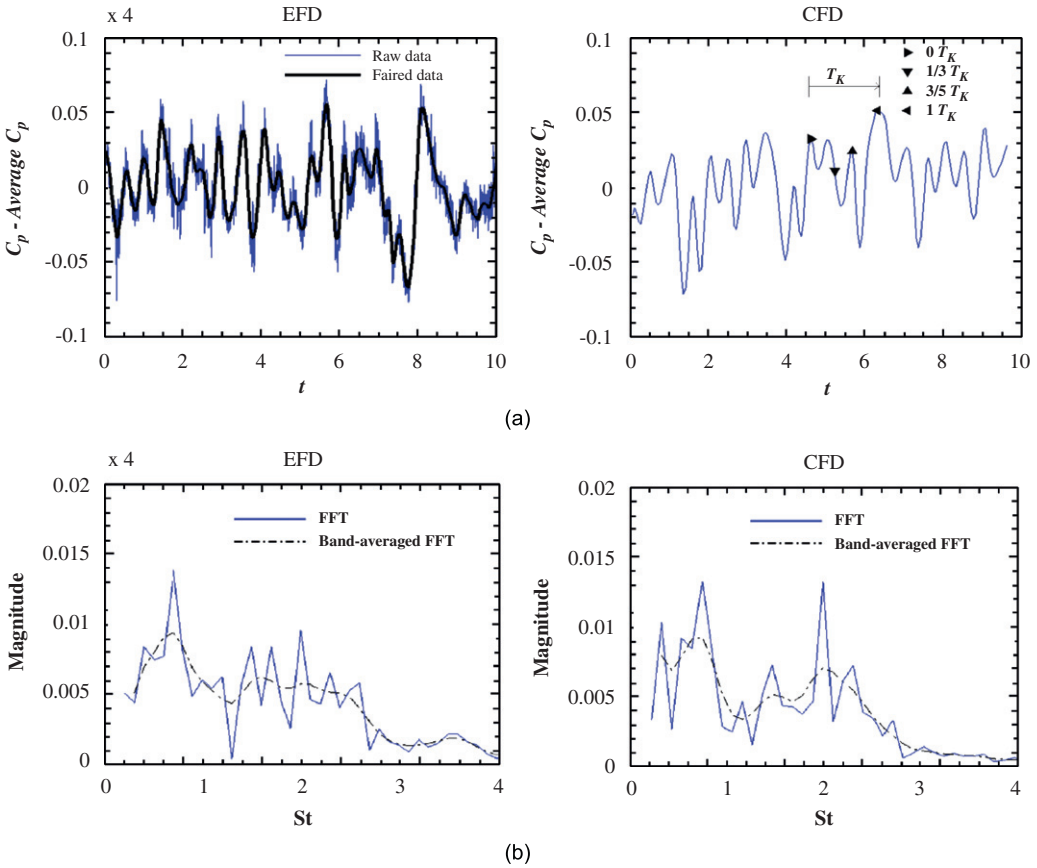

Fig. 9. Validation of unsteady C_P at location of dominant Karman-like instability ($x = 0.86$, $z = -0.14$) denoted by the diamond location marker in Fig. 7(b): (a) time history; CFD time markers indicate instances at which detailed volume flow will be presented in Fig. 14; (b) frequency spectra.

shear-layer vortices; these vortices amalgamate to form the Karman-like vortices, which interact with their mirror image and shed immediately after the reattachment point. Meanwhile, the stationary recirculation bubble experiences a periodic enlargement and shrinkage due to the flapping instability.

5.1. Shear-layer instability

Figs. 12(a)–(d) illustrate the CFD volume solutions at time steps corresponding to the time markers in Fig. 8. The circle location markers indicate the location at which the C_P time histories and frequency spectra are presented in Fig. 8. The vortex core lines are contoured by the nondimensional vortex strength. The skin friction lines and free surface streamlines are also shown. The recirculation region on the free surface will be termed the primary closed separation. The spiral node N1 denotes the initial stage of the shear-layer vortex formation. The separatrices, namely LS2 (line of separation) and LA2 (line of attachment), converge at saddle point S2 and enclose the primary closed separation (Fig. 12(a)). LA2 terminates at node Na at the reattachment point. LS2 and LA2 form a wedge-shaped dividing surface, which is not closed with respect to N1, as LS2 does not reach the free surface, but rather terminates at N1. As N1 convects downstream, the wedge opens up, allowing the shear-layer vortex to enter the recirculation region and merge with the vortex in the recirculation region (Fig. 12(b)). The convection of the node N1 causes the saddle S1 attached with this node to convect downstream. Similar to S2, the saddle S1 has two separatrices, LS1 and LA1. LA1 also terminates at Na. As N1 convects downstream, the wedge enclosed by LA1 and LS1 enlarges separating N1 from the primary closed separation (Fig. 12(c)) and the vortex connecting N1 with the outward spiral node on the free surface breaks down. LS1 terminates at the newly

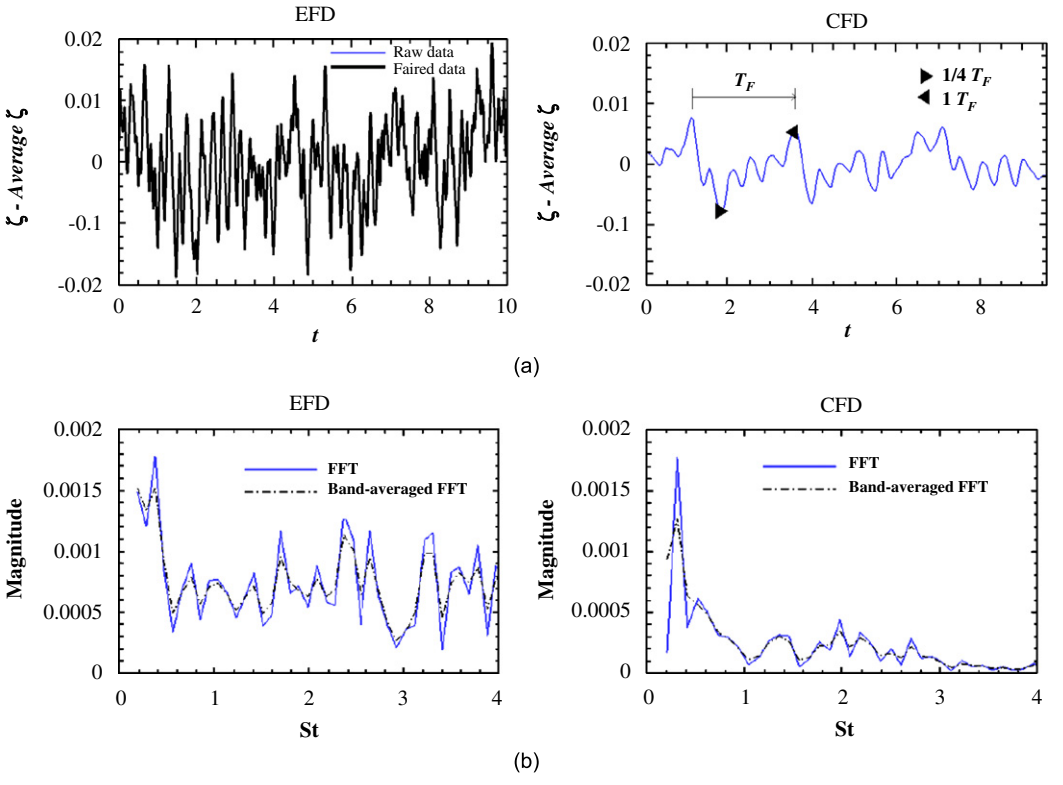

Fig. 10. Validation of unsteady ζ at location of dominant flapping instability ($x = 0.90$, $y = 0.32$) denoted by the square marker in Fig. 5(b): (a) time history; CFD time markers indicate instances at which flow details will be presented in Fig. 15; (b) frequency spectra.

formed spiral node N0 (shear-layer vortex) to which the LS1, LA1 wedge enclosure is open (Fig. 12(d)) and the cycle repeats.

The above described process occurs periodically with St = 2. The shear-layer roll up is evident only on the foil surface skin friction lines and not on the free surface streamlines. However, the low-pressure field created by the vortex core causes the free surface to depress along the vortex path causing the shoulder waves with St = 2, which show up as the dominant St contours on the free surface within the separation region (Fig. 5(b)). θ and U_S were evaluated at the separation starting point to get the normalized Strouhal number St_θ. $U_S = 1.45$ and $\theta = 0.0028$, which gives $St_\theta = 0.00386$.

Ripley and Pauley (1993) showed computationally that St_θ remains almost constant over a range of Re for the case of laminar flow past an airfoil ($St_\theta = 0.0056 \pm 2\%$). However, St_θ showed a 16% reduction compared to previous simulations on a different geometry and they concluded that St_θ is dependent on the C_P distribution. Current 2-D laminar simulations at Re = 1500 and 2500 gave $St_\theta = 0.0063$ and 0.00615, respectively, indicating a 2% difference. The laminar solutions at Fr = 0.37 indicated a change in C_P distribution due to the free surface waves, but St_θ did not change significantly (less than 5% difference compared to the 2-D simulations). However, St_θ for the turbulent Fr = 0.37 simulation indicates a significant reduction of about 40% compared to the laminar cases. The turbulent boundary layer requires a higher adverse pressure gradient to separate. Based on Ripley and Pauley's observation that St_θ is a function of the non-dimensional pressure distribution, the current results suggest that St_θ varies inversely with the non-dimensional adverse pressure gradient at separation.

The Brown and Lopez (1990) criterion for vortex breakdown in swirling flows states that for breakdown to occur, the helix angle of velocity should exceed that of vorticity along some stream surface (necessary, but not sufficient condition). If $\delta = \tan^{-1}(v/w) - \tan^{-1}(\eta/\zeta)$, where the ratios ($v$/w) and ($\eta/\zeta$) are of the azimuthal and axial components of velocity and vorticity respectively, then δ has to be positive in order for breakdown to occur. Contours of δ along the vortex core (Fig. 13) show that the criterion is satisfied with the breakdown occurring at maximum positive δ (= 0.4) on the core. Fig. 13 also shows the diverging streamlines and stagnation in the vortex core at the breakdown point with the flow converging from the top and bottom.

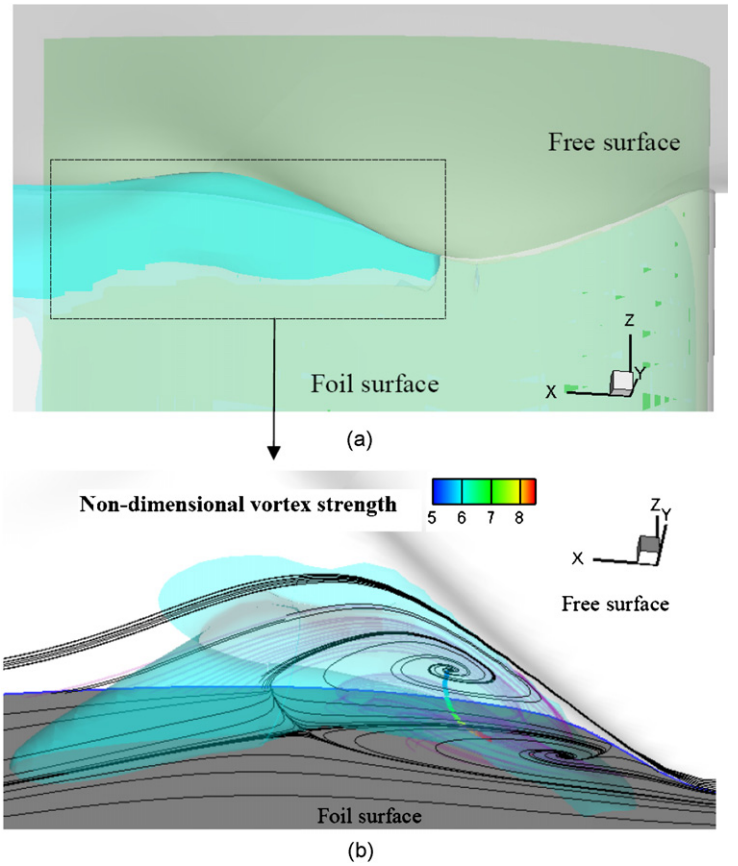

Fig. 11. Mean separation pattern: (a) iso-surface of stagnation C_P (= 0.29); (b) close-up view of separation region showing vortex core line colored by vortex strength; iso-surfaces of $Q = 1$; and surface and volume streamlines.

5.2. *Karman-like instability*

Figs. 14(a)–(d) illustrate the CFD volume solutions at time steps corresponding to the time markers in Fig. 9(a). The diamond location markers indicate the location at which the C_P time histories and frequency spectra are presented in Fig. 9. Here the amalgamation of the shear-layer vortices produces a relatively weak vortex, since it occurs after the vortex breakdown, which causes an appreciable dissipation. The artificial dissipation of the shear-layer vortices prior to their amalgamation caused by URANS also contributes to the diminished strength of the predicted Karman-like vortices. The velocity vector eigen-mode method for core extraction fails to capture the vortex filaments after breakdown. However, the iso-surface of positive Q indicates the behavior of vortical structures over one Karman-like shedding period. Figs. 14(a) and (b) illustrate the Karman-like vortex shedding (V_{shed}) at the beginning of the cycle. Figs. 14(b) and (c) illustrate the amalgamation of the shear-layer vortices V1, V2, and V3. Fig. 14(d) illustrates the shedding of the Karman-like vortex after the amalgamation of the shear-layer vortices, thus completing the cycle. This process occurs quasi-periodically with St$\sim$0.74 which shows up in the dominant St contours on the foil surface and free surface immediately after reattachment. The normal distance of the separated shear layer from the foil at the free surface, used as the equivalent for half-wake thickness ($h = 0.13$), gives $St_h = 0.066$.

Investigation of the laminar solutions at Fr = 0.37 showed that the deep flow exhibits periodic asymmetric Karman vortex shedding with $St_h = 0.08$ similar to the 2-D laminar results. At the free surface, the vortices are unsteady, but a clear periodic shedding was not evident. St_h was calculated based on the frequency of unsteadiness at the free surface and was found to be 0.069. The free surface decreases St_h, but St_h remains relatively unaffected compared to the turbulent solution. The decrease in St_h near the free surface is presumably due to the inclination of the separated shear layer and the induced three-dimensionality, which causes the interaction of the opposite vortices to become less prominent.

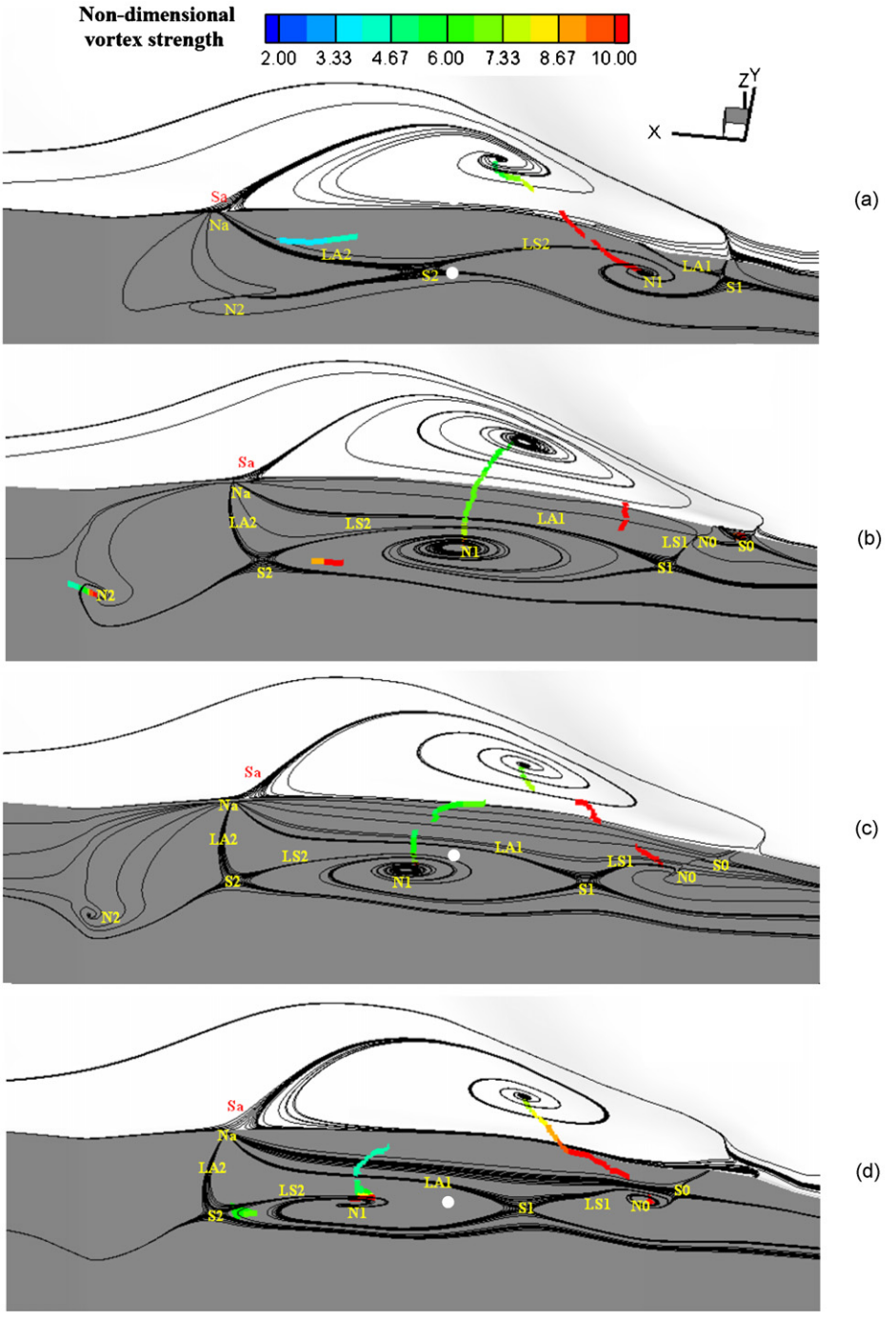

Fig. 12. Instantaneous separation pattern over one shear-layer vortex shedding period displaying vortex cores at time steps corresponding to the time markers on the CFD C_P time-history plot in Fig. 8(a); the circle location marker indicates the location at which the C_P time history is presented in Fig. 8(a): (a) 0 T_S, (b) 3/5 T_S, (c) 3/4 T_S, and (d) 9/10 T_S.

5.3. *Flapping instability*

The free surface bubble exhibits a periodic increase and decrease in size with St = 0.32. The ζ magnitudes are larger when the bubble size is smaller and *vice versa*, demonstrating a standing-wave-type nature. This standing wave with

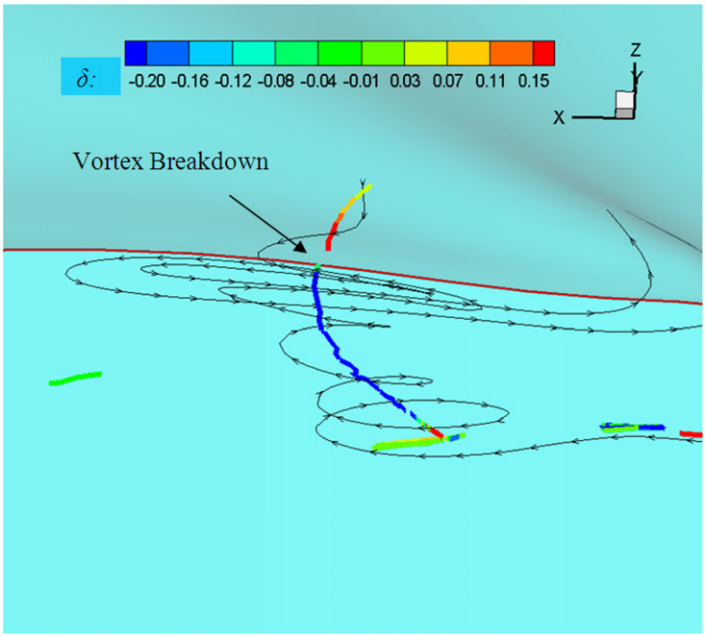

Fig. 13. Contour plots of δ at instance of vortex breakdown.

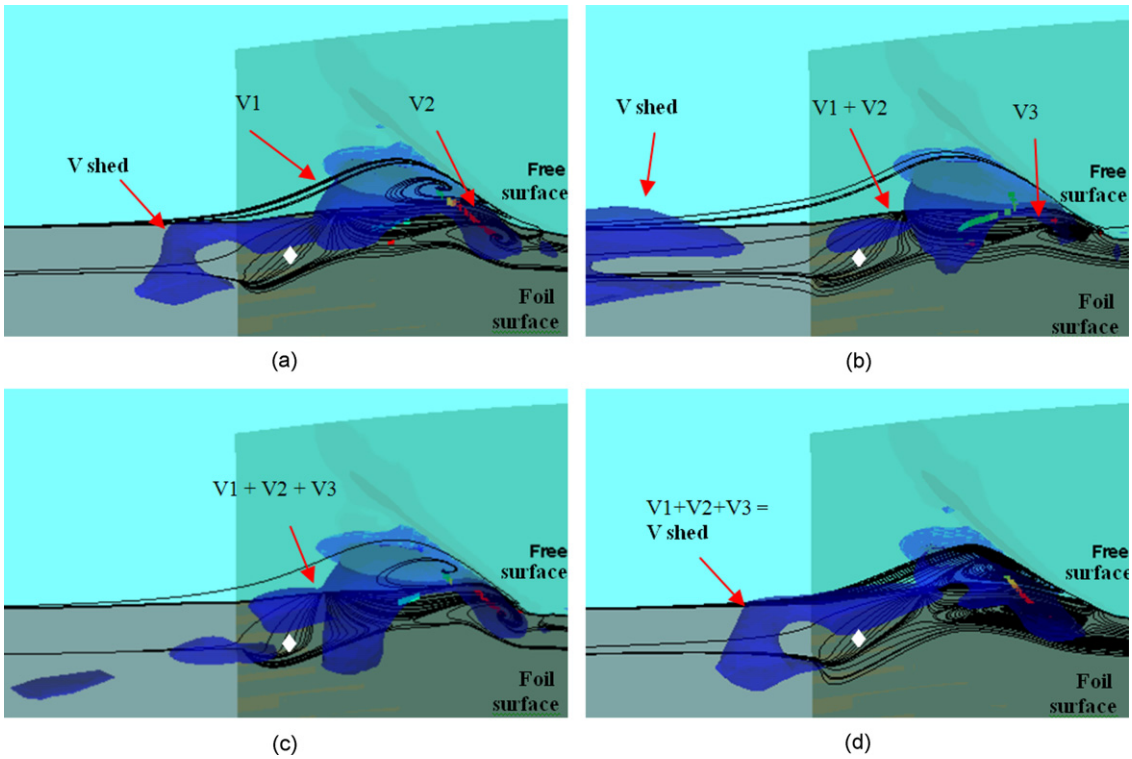

Fig. 14. Instantaneous separation pattern over one Karman-like vortex shedding period displaying iso-surfaces of $Q = 1$ at time steps corresponding to the time markers on the CFD C_P time-history plot in Fig. 9(a); the diamond location marker indicates the location at which the C_P time history is presented in Fig. 9(a): (a) 0 T_K, (b) 1/3 T_K, (c) 3/5 T_K, and (d) 1 T_K.

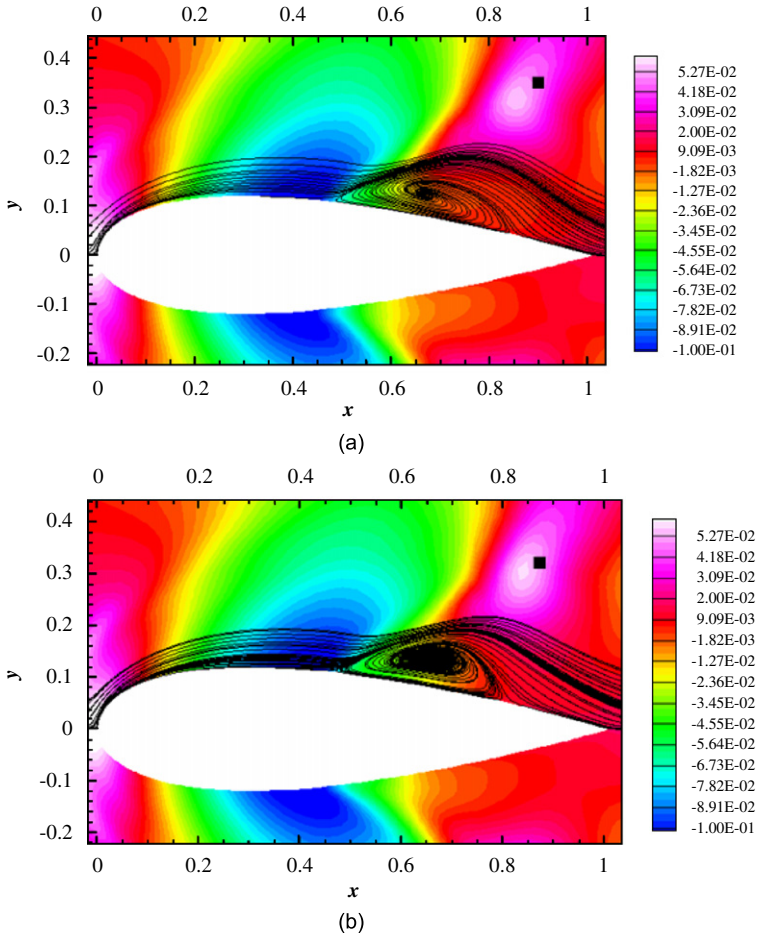

Fig. 15. Free surface streamlines showing extremities of the bubble size corresponding to the flapping instability at time steps corresponding to the time markers on the CFD ζ time-history plots shown in Fig. 10(a); the square location marker indicates the location at which the ζ time history is presented in Fig. 10(a): (a) $\frac{1}{4}T_F$ and (b) $1T_F$.

$\mathrm{St} = 0.32$ shows up in the dominant St contours on the free surface, outside the separation bubble (Fig. 5(b)). Fig. 15 shows two extremities of the bubble size at time steps corresponding to the time markers in Fig. 10(a). The square location markers indicate the location at which the ζ time histories and frequency spectra are presented in Figs. 10(a) and (b), respectively. The reattachment point oscillates between $x = 0.79$ and 0.84. The mean reattachment length X_R is 0.42 giving $\mathrm{St}_R = 0.13$. The oscillation of the instantaneous reattachment point indicates an oscillation of 0.12 X_R about the mean X_R.

6. Conclusions

The applicability of URANS with a surface-tracking method to predict the vortical structures and instabilities has been investigated for unsteady free surface wave-induced separation. Quantitative verification and validation studies were conducted. The mean flow solutions for the free surface wave-elevation and foil surface pressure show good correspondence with the EFD, the main shortcoming being that URANS predicts higher wave-elevation magnitudes, and predicts a quicker pressure recovery after separation. The mean separation pattern shows a reattaching flow with wall-bounded separation bubble. URANS proved capable in predicting the three main instabilities expected for reattaching flows, namely the initial shear-layer instability causing the initial roll up of the shear-layer vortices, the Karman-like shedding, which occurs after the merger of the shear-layer vortices, and the flapping of the separation bubble. FFT of both ζ and the foil surface C_P showed three distinct dominant frequency regions corresponding to the

three instabilities. The r.m.s. of the free-surface oscillations indicates an initial amplitude defect of 30% where the shear layer separates, and the defect progressively increases downstream as URANS rapidly dissipates the rolled up vortices. The point-wise C_P frequency spectra on the foil surface at the shear-layer and Karman-like instability dominant regions show an amplitude defect of 50% and 75%, respectively.

One main difference between the vortex dynamics of the present case and other reattaching separated flows like backward-facing steps and flow past leading blunt edge of circular cylinders is the relatively weaker Karman-like shedding in the present case evident from both EFD and CFD. This is due to the comparatively shorter reattachment length for the current case ($X_R = 0.4L$) which allows for the amalgamation of just two or three shear-layer vortices prior to shedding. Flow past leading blunt edge of circular cylinders has a longer reattachment length ($X_R = 10R_C$) which allows for a higher amplification due to amalgamation of 10–20 shear-layer vortices (Sigurdson, 1995). URANS further diminishes the strength of the predicted Karman-like vortices due to the rapid dissipation of the shear-layer vortices before amalgamation.

The normalized frequencies based on relevant length scales for the shear-layer and Karman-like instability were investigated for both laminar and turbulent cases at Fr = 0.37. For the shear-layer instability, St_θ for the turbulent case is 40% lower than the laminar cases, suggesting that St_θ varies inversely with the non-dimensional adverse pressure gradient at separation. The deep flow in the laminar flow solutions exhibits asymmetric Karman shedding with St_h in agreement with the universal value of 0.08, but near the free surface St_h decreases to 0.069. For the turbulent solutions, the deep flow is attached and the free surface flow exhibits Karman-like shedding with $\mathrm{St}_h = 0.066$. The inclination of the separated shear layer at the free surface, and the resulting reduction in interaction between the opposite vortices is conjectured to be the cause of the reduced St_h for both the laminar and the turbulent cases. St_R for the flapping instability is comparable to that observed for backward-facing steps and blunt cylinders.

The complementary DES study (Xing et al., 2007) supports many of the findings from URANS. The global topology of the mean flow was similar to URANS, showing similarity to the owl-face pattern. The mean DES volume flow solutions showed a similar inverted "V" shape vortical flow pattern as seen from the URANS solutions with the upstream leg depicting the mean of the shear-layer vortices and the downstream leg depicting the mean of the Karman-like vortices. The DES solutions have broader frequency spectra for the free surface wave-elevation and foil surface pressure, but they do show similar dominant frequencies as URANS without the amplitude defect. The comparisons with DES and EFD indicate that URANS resolves the organized oscillations due to the large-scale vortical structures and instabilities, but with deficiency in their amplitudes thereby capturing the gross features of the unsteady separation.

DES overcomes the amplitude deficiency, but similar to the EFD, the numerous small-scale vortices in the separation region make isolation, visualization, and analysis of the large-scale vortical structures difficult. Phase averaging the DES solutions would enable clearer identification of the organized oscillations, but the presence of multiple dominant periodic modes with nonlinear interactions with each other makes this difficult. In the present study, the smoother flow field due to the inherent time averaging of the URANS model enabled isolation of the large-scale vortical structures.

Acknowledgments

The Office of Naval Research under Grant N00014-01-1-0073, administered by Dr Patrick Purtell, sponsored this research.

References

Brocchini, M., 2002. Free surface boundary conditions at a bubbly/weakly splashing air–water interface. Physics of Fluids 14 (6), 1834–1840.

Brocchini, M., Peregrine, D.H., 2001. The dynamics of strong turbulence at free surfaces. Part 1. Description. Journal of Fluid Mechanics 449, 225–254.

Brown, G.L., Lopez, J.M., 1990. Axisymmetric vortex breakdown: part 2 physical mechanisms. Journal of Fluid Mechanics 221, 553–576.

Carrica, P.M., Wilson, R.V., Stern, F., 2006. An unsteady single-phase level-set method for viscous free surface flows. International Journal of Numerical Methods in Fluids 53, 229–256.

Chow, S.K., 1967. Free surface effects on boundary layer separation on vertical struts. Ph.D. Thesis, The University of Iowa.

Constantinescu, G.S., Chapelet, M.C., Squires, K.D., 2003. Turbulence modeling applied to flow over a sphere. AIAA Journal 41 (9), 1733–1742.

Hunt, J.C.R., Wray, A.A., Moin, P., 1988. Eddies, stream, and convergence zones in turbulent flows. Report CTR-S88, Center for Turbulence Research, Stanford University, Stanford, CA 94305–3035.

Johnson, D.A., Menter, F.R., Rumsey, C.L., 1994. The status of turbulence modeling for aerodynamics. AIAA Paper No. 1994-2226.
Kandasamy, M., 2001. RANS simulation of free surface wave-induced separation around a surface-piercing NACA-0024 hydrofoil. M.S. Thesis, The University of Iowa.
Kandasamy, M., 2005. URANS for unsteady free surface wave-induced boundary layer separation. Ph.D. Thesis, The University of Iowa.
Kawamura, T., Mayer, S., Garapon, A., Srensen, L., 2002. Large eddy simulation of a flow past a free surface-piercing circular cylinder. ASME Journal of Fluids Engineering 124, 91–101.
Khorammi, M.R., Singer, B.A., Berkman, M.E., 2001. Time-accurate simulations and acoustic analysis of slat free-shear-layer. In: 7th AIAA/CEAS Aeroacoustics Conference, AIAA Paper No. 2001-2155.
Kiya, M., Sasaki, K., 1985. Structure of large-scale vortices and unsteady reverse flow in the reattaching zone of a turbulent separation bubble. Journal of Fluid Mechanics 154, 463–491.
Lee, I., Sung, H.J., 2002. Multiple-arrayed pressure measurement for investigation of the unsteady flow structure of a reattaching shear-layer. Journal of Fluid Mechanics 463, 377–402.
Lin, P., Li, C.W., 2003. Wave–current interaction with a vertical square cylinder. Ocean Engineering 30, 855–876.
Liu, Y.Z., Ke, F., Sung, H.J., 2008. Unsteady separated and reattaching turbulent flow over a two-dimensional square rib. Journal of Fluids and Structures 24, 366–381.
Menter, F.R., 1994. Two equation eddy viscosity turbulence models for engineering applications. AIAA Journal 32 (8), 1598–1605.
Metcalf, B., 2001. Experimental investigations on free surface wave-induced separation. M.S. Thesis, The University of Iowa.
Metcalf, B., Longo, J., Ghosh, S., Stern, F., 2006. Unsteady free surface wave-induced boundary-layer separation for a surface-piercing NACA 0024 foil: towing tank experiments. Journal of Fluids and Structures 22, 77–98.
Miksad, R.W., Jones, F.L., Powers, E.J., Kim, Y.C., Khadra, L., 1982. Experiments on the role of amplitude and phase modulations during transition to turbulence. Journal of Fluid Mechanics 123, 1–30.
Paik, J., Ge, L., Sotiropoulos, F., 2004. Toward the simulation of complex 3-D shear flows using unsteady statistical turbulence models. International Journal of Heat and Fluid flows 25, 513–527.
Perry, A.E., Chong, M.S., 1987. A description of eddying motions and flow patterns using critical-point concepts. Annual Review of Fluid Mechanics 19, 125–155.
Pogozelski, E.M., Katz, J., Huang, T.T., 1997. The flow structure around a surface-piercing strut. Physics of Fluids 5, 1387–1399.
Post, H., Vrolijk, B., Hauser, H., Laramee, R.S., Doleisch, H., 2003. The state of the art in flow visualization: feature extraction and tracking. Computer Graphics Forum 22 (4), 775–792.
Prasad, A., Williamson, C.H.K., 1997. The instability of the hear layer separating from a bluff body. Journal of Fluid Mechanics 333, 375–402.
Ripley, M.D., Pauley, L.L., 1993. The unsteady structure of two-dimensional steady laminar separation. Physics of Fluids A 5 (12), 3099–3106.
Roshko, A., 1955. On the wake and drag of bluff bodies. Journal of Aeronautical Sciences 22, 124–135.
Sigurdson, L.W., 1995. The structure and control of turbulent reattaching flow. Journal of Fluid Mechanics 248, 139–165.
Sotiropoulos, F., Abdallah, S., 1992. A primitive variable method for the solution of three dimensional incompressible viscous flows. Journal of Computational Physics 103, 336–349.
Stern, F., Hwang, W.S., Jaw, S.Y., 1989. Effects of waves on the boundary layer of a surface-piercing flat plate: experiment and theory. Journal of Ship Research 33, 63–80.
Stern, F., Choi, J.E., Hwang, W.S., 1993. Effects of waves on the wake of a surface-piercing flat plate: experiment and theory. Journal of Ship Research 33, 102–118.
Stern, F., Wilson, R.V., Coleman, W., Patterson, G., 2001. Computational approach to verification and validation of CFD simulation—part 1: methodology and procedures. ASME Journal of Fluids and Engineering 123, 793–802.
Sujudi, D., Haimes, R., 1995. Identification of swirling flow in 3-D vector fields. In: AIAA 12th Computational Fluid Dynamics Conference, Paper No. 95-1715.
Williamson, C.H.K., 1996. Vortex dynamics in the cylinder wake. Annual Review of Fluid Mechanics 28, 477–526.
Wilson, R., Shao, J., Stern, F., 2004. Discussion: criticisms of the "correction factor" verification method. ASME Journal of Fluids Engineering 126, 704–706.
Wilson, R.V., Carrica, P.M., Stern, F., 2006. Unsteady RANS method for ship motions with application to roll for a surface combatant. Computers and Fluids 35 (5), 501–524.
Xing, T., Kandasamy, M., Stern, F., 2007. Unsteady free surface wave-induced separation: analysis of turbulent structures using detached eddy simulation and single phase level-set. Journal of Turbulence 8 (44), 1–35.
Zhang, Z., Stern, F., 1996. Free surface wave-induced separation. ASME Journal of Fluids Engineering 118, 546–554.